Noninvasive high-frequency oscillations riding spikes delineates epileptogenic sources

Zhengxiang Cai[a], Abbas Sohrabpour[a], Haiteng Jiang[a], Shuai Ye[a], Boney Joseph[b,c], Benjamin H. Brinkmann[b,c], Gregory A. Worrell[b,c], and Bin He[a,1]

[a]Department of Biomedical Engineering, Carnegie Mellon University, Pittsburgh, PA 15213; [b]Department of Neurology and Physiology, Mayo Clinic, Rochester, MN 55905; and [c]Department of Biomedical Engineering, Mayo Clinic, Rochester, MN 55905

Edited by Emery N. Brown, Massachusetts General Hospital, Boston, MA, and approved March 8, 2021 (received for review May 31, 2020)

High-frequency oscillations (HFOs) are a promising biomarker for localizing epileptogenic brain and guiding successful neurosurgery. However, the utility and translation of noninvasive HFOs, although highly desirable, is impeded by the difficulty in differentiating pathological HFOs from nonepileptiform high-frequency activities and localizing the epileptic tissue using noninvasive scalp recordings, which are typically contaminated with high noise levels. Here, we show that the consistent concurrence of HFOs with epileptiform spikes (pHFOs) provides a tractable means to identify pathological HFOs automatically, and this in turn demarks an epileptiform spike subgroup with higher epileptic relevance than the other spikes in a cohort of 25 temporal epilepsy patients (including a total of 2,967 interictal spikes and 1,477 HFO events). We found significant morphological distinctions of HFOs and spikes in the presence/absence of this concurrent status. We also demonstrated that the proposed pHFO source imaging enhanced localization of epileptogenic tissue by 162% (~5.36 mm) for concordance with surgical resection and by 186% (~12.48 mm) with seizure-onset zone determined by invasive studies, compared to conventional spike imaging, and demonstrated superior congruence with the surgical outcomes. Strikingly, the performance of spike imaging was selectively boosted by the presence of spikes with pHFOs, especially in patients with multitype spikes. Our findings suggest that concurrent HFOs and spikes reciprocally discriminate pathological activities, providing a translational tool for noninvasive presurgical diagnosis and postsurgical evaluation in vulnerable patients.

high-frequency oscillations | epilepsy | electrophysiological source imaging | electrophysiology

Epilepsy affects around 70 million people globally (1). About one-third of the patients have medically refractory epilepsy and may undergo surgical resection to control or stop seizures (2, 3) if the epileptogenic zone (EZ, the brain area and connections required for seizure generation) can be accurately localized. The current clinical gold standard is to use seizure-onset zone (SOZ), which is routinely determined by the intracranial electroencephalography (iEEG) during multiple-day invasive monitoring for the occurrence of spontaneous seizures (2), as an approximation of the EZ. Although successful in many patients, iEEG is limited to regional sampling and typically involves extreme discomfort and increased deleterious risk associated with chronically implanted electrodes due to its invasive nature (4, 5). It is therefore highly desirable to seek noninvasive approaches to localize and image the EZ, particularly from widely accessible scalp EEG recordings.

High-frequency oscillations (HFOs), including ripples (80 to 250 Hz) and fast ripples (250 to 500 Hz), have been widely proposed as a promising electrophysiological biomarker of the EZ (6, 7) and SOZ (8, 9). Originally observed in human hippocampal recordings (10), subsequently in neocortex recordings (8), and most recently in scalp EEG recordings (11, 12), HFOs are defined as spontaneous oscillatory activities (above 80 Hz) standing out from the background and persisting for at least four oscillation cycles (13). In the epileptogenic brain, HFOs has been correlated with ictogenesis (14), and the removal of brain areas containing HFOs is found to improve surgical outcomes (15–17), which may be more accurate than the irritative zone (IZ, also known as spike-generating zone) (18) or even the SOZ (19).

However, the clinical translation of noninvasively recorded HFOs has been impeded by several challenges (7, 20). First of all, there are physiological HFOs (21) and spurious artifacts (13, 22) that could mimic the presence of pathological HFOs and share the same frequency range (23, 24), which complicates the distinction of clinically relevant HFOs from artifactual or normal ones (25). When defined only by the occurrence rate, physiological HFOs cannot be disentangled from the pathological ones, which might reduce the specificity of HFOs to epileptic areas (26, 27) or even result in conflicting findings (28, 29). Recent studies have shown significant spatiotemporal overlap between HFOs and interictal epileptiform spikes (20), with a higher association to the epileptogenic regions compared to spikes or HFOs alone, promising an improved biomarker to epileptogenicity (12, 30, 31). These concurrent activities are reported to have good prediction of seizure risk (32–34) and postsurgical cognitive improvement (35). However, to identify this biomarker, visual marking is still commonly adopted, which is highly time and labor consuming and prone to subjective biases (36, 37). While several scalp HFO detectors have

Significance

Millions of people affected by epilepsy may undergo surgical resection of the epileptic tissues to stop seizures if such epileptic foci can be accurately delineated. High-frequency oscillations (HFOs), existing in electroencephalography, are highly correlated with epileptic brain, which is promising for guiding successful neurosurgery. However, it is unclear whether and how pathological HFOs can be differentiated to localize the epileptogenic tissues given the presence of various nonepileptic high-frequency activities. Here, we show morphological and source imaging evidence that pathological HFOs can be identified by the concurrence of epileptiform spikes. We describe a framework to delineate the underlying epileptogenicity using this biomarker. Our work may offer translational tools to improve treatments by noninvasively demarking pathological activities and hence epileptic foci.

Author contributions: Z.C. and B.H. designed research; Z.C., A.S., H.J., S.Y., B.J., B.H.B., G.A.W., and B.H. performed research; Z.C., G.A.W., and B.H. contributed new reagents/analytic tools; Z.C. analyzed data; Z.C., A.S., B.H. wrote the paper; and B.H. supervised the research.

Competing interest statement: Z.X. and B.H. are coinventors of a patent application filed by Carnegie Mellon University on some algorithms that were used in this work.

This article is a PNAS Direct Submission.

[1]To whom correspondence may be addressed. Email: bhe1@andrew.cmu.edu.

This article contains supporting information online at https://www.pnas.org/lookup/suppl/doi:10.1073/pnas.2011130118/-/DCSupplemental.

Published April 19, 2021.

been proposed (38–40), these approaches are semiautomated and require expert review to achieve optimal performance. On the other hand, electrophysiological source imaging (ESI) is an approach to estimate the underlying brain electrical activity from scalp electromagnetic measurements (41, 42). It is highly desirable to localize the epileptic brain and delineate the EZ using scalp-recorded HFOs via ESI, while it is also challenging due to the high noise level existing in the high-frequency band in scalp recordings (20).

What remains to be achieved in the current clinical practice is a tractable and robust means to identify pathological HFOs from noninvasive EEG and localize the underlying epileptic tissue from scalp recordings at the individual patient level. Recently, invasive studies have suggested that epileptic HFOs are highly associated with repetitive and morphological patterns in both low- and high-frequency bands (43, 44). On the other hand, renewed interest has been given to subgroups of spikes conceptualized as "green" and "red" spikes, classifying those less and more likely to index epileptogenic tissue (45), since spikes generally have low specificity to the EZ and are nonunitary in nature (24, 46). In line with this notion, we introduce an approach for automatic identification of pathological HFOs by integrating two premises of epileptiform pathology, 1) concurrence with interictal spikes and 2) repetitive appearance, to assist the discrimination of epileptic from nonepileptic activities. The central hypothesis of this study is that the concurrence of HFOs on spikes identifies a subtype of pathological HFOs by which the EZ can be delineated, and, in turn, it demarks a spike subgroup which may account for the higher degree of epileptic significance than the general population of spikes (Fig. 1).

In the present study, we have developed an approach to automatically identify the scalp-recorded HFOs consistently co-occurring with epileptiform spikes and image the corresponding cortical sources generating these events using ESI techniques (Fig. 1 *A* and *B*), and we investigated the morphological characteristics of HFOs and spikes in the presence or absence of this concurrent phenomenon. We further validated the clinical value of using the identified HFOs in determining the underlying epileptogenicity against the clinical findings defined by epileptologists and the surgical outcomes with comparison to the conventional spike-imaging method (Fig. 1 *B* and *C*).

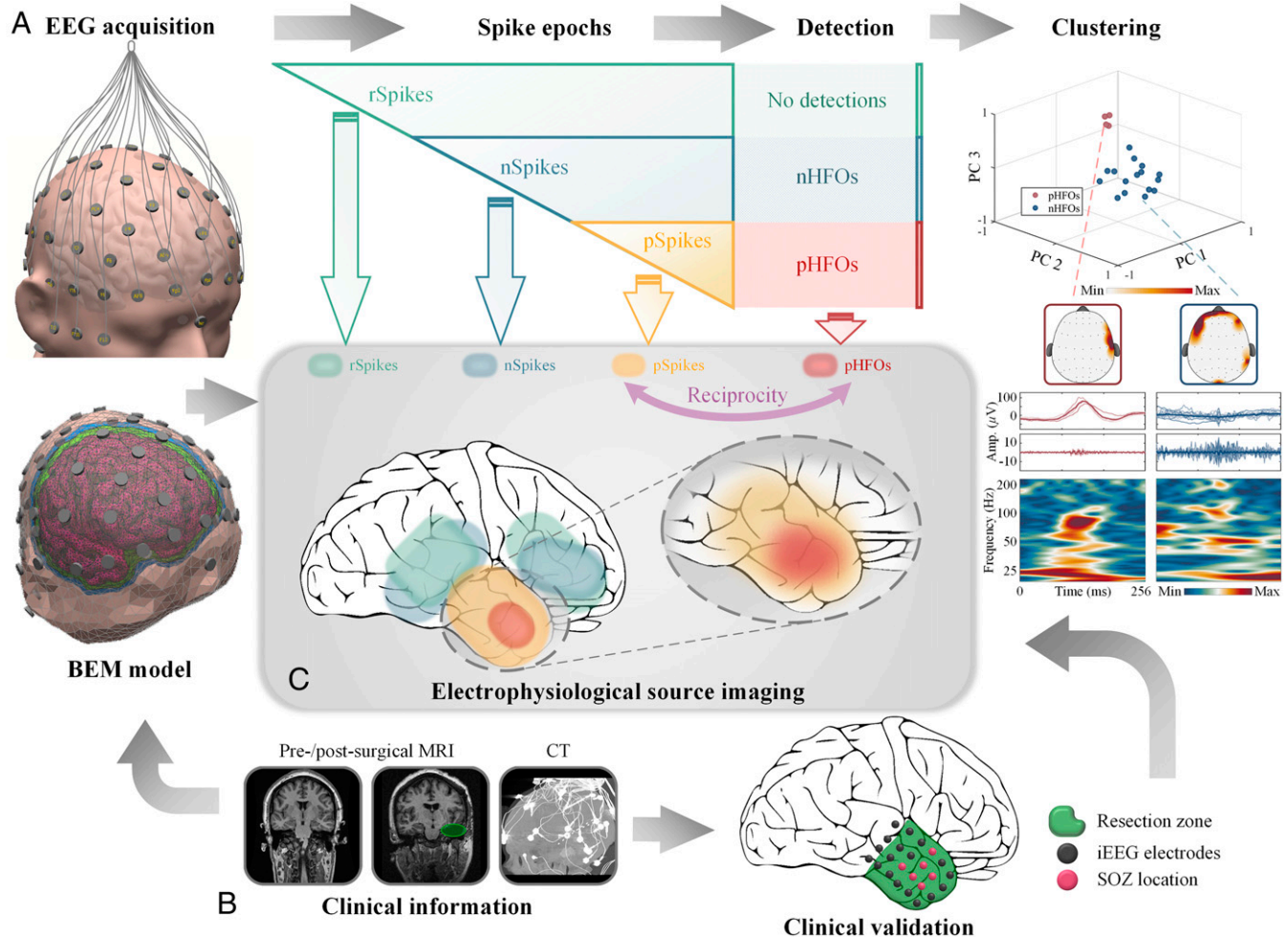

Fig. 1. Conceptual diagram of data analysis and hypothesis. (*A*) EEG data analysis workflow. Spike epochs are collected from high-density (76-channel) EEG in each patient, and HFOs are identified through a detection and clustering process to determine pHFOs and nHFOs, which in turn separates spike population into three subgroups (p/n/rSpikes). Examples of clustered p/nHFOs in a representative patient (P1) are illustrated with scalp topology, raw and filtered (>80 Hz) signals, and time-frequency representations (see also examples in Fig. 2). (*B*) Clinical evidence and modeling. Presurgical MRI is used to build a realistic head model for individual patients using boundary element model (BEM), postsurgical MRI is for modeling the surgical resection zone (green), and computed tomography (CT) images are used to localize the iEEG implantation (black) from which the SOZ (pink) is defined by the clinicians. (*C*) Hypothesized reciprocity between HFOs and spikes. We hypothesize that the pHFOs with concurrent pSpikes are pathological activities by which the underlying tissue epileptogenicity can be delineated via ESI techniques, and in turn the pSpikes, selected by pHFOs, are more specific to the epileptic tissue than the general population of spikes.

Results

Identification of Interictal Spikes and HFOs. We recorded high-density (76-channel) EEG from 25 patients with temporal lobe epilepsy (TLE) during long-term presurgical monitoring. For each patient, typical forms of interictal spikes were identified by a board-certified epileptologist and later verified by another with consensus on the occurrence, spatial location, and morphology of the spikes. We also applied a commonly adopted and well-validated commercial software, Persyst 13 (Persyst Development Corporation) (47), for automated spike detection to optimize identification of spikes in each patient. Upon the spike detections from Persyst, we manually screened all these events, discarded the spurious ones, and grouped the remaining into spike types according to distinct spatiotemporal patterns of the typical spike forms for each patient. Across all patients, a total of 2,967 spikes were identified. The average number of distinct spike types per patient was 2.2 ± 1.2 (mean ± SD, $n = 25$) for all patients and 2.7 ± 1.1 for patients with multiple (more than one) spike types (MST, $n = 18$). Patients with MST accounted for 67% of the seizure-free cohort ($n = 18$) and 86% of the non–seizure-free cohort ($n = 7$). Moreover, the number of spike types in the non–seizure-free cohort was significantly higher compared to the seizure-free cohort ($P = 0.015$, $d = 1.1$, two-sided Student's t test), suggesting a correlation between the severity of epileptic disorder and the range of spike foci (48). In addition, we recorded four patients with extratemporal lobe epilepsy (ETLE) for case studies, and the same analysis approach was applied in line with the TLE patients. Detailed patient information and surgical outcome can be found in *Materials and Methods* and *SI Appendix*, Tables S1 and S2.

All identified spikes were extracted as 1 s epochs for automatic detection of HFOs (*Materials and Methods* and *SI Appendix*, Fig. S1). The adopted approach was designed to capture and distinguish stereotyped HFOs with consistent and repetitive patterns (i.e., ripples riding on spikes, also known as spike ripples) based on the commonly accepted concepts in clinical studies about pathological HFOs (11, 13). The efficacy of the proposed detector in successfully identifying HFOs from various artifactual and noisy high-frequency activities (HFAs) was evaluated through a Monte Carlo simulation with realistic EEG signals and brain models derived from clinical data in human subjects (49), and the proposed method was compared against a well-established benchmark detector (32, 39) (*SI Appendix*, Text S2 and Figs. S2 and S3). In total, 1,477 high-frequency events were identified (from 1,065 spike epochs) across all patients, and in each patient, about 18.1 ± 12.0% (mean ± SD, $n = 25$) are positive HFOs (pHFOs, events with repetitive patterns and riding on spikes or spike ripples), and 81.9 ± 12.0% are negative HFOs (nHFOs, events without consistency on spikes). Examples of clustered HFO detections are shown in Fig. 2, and *SI Appendix*, Fig. S6*A* depicts results for ETLE.

Morphological Characteristics of HFOs. We investigated whether consistent spatiotemporal distinctions exist between pHFOs of putative pathology and nHFOs across all patients. First, we observed that the spatial distribution of electrodes containing pHFOs was focal and constrained on the scalp (50, 51), and the waveforms of pHFOs in both raw and high-pass filtered signals were uniform and stereotypical, while nHFOs were spatially widespread with the irregular waveforms (43) (Fig. 2). Note that pHFOs were highly associated with the spike profile, while nHFOs were generally discordant with the spike either temporally or spatially. To quantify such differences, corresponding temporal analysis demonstrated that pHFOs had a significantly higher peak in the amplitude of z-scored power compared to nHFOs ($n = 25$; $P = 0.0062$, $d = 0.84$, two-sided Mann–Whitney U test; Fig. 3 *A*–*C*), indicating a prominent burst around the pHFO peak relative to a clear background, while nHFOs have less separation from the elevated background (Fig. 3 *A* and *B*) (44, 52). The spectral analysis revealed that the median frequency of pHFOs was significantly lower than that of nHFOs ($n = 25$; $P = 0.0054$, $d = 0.38$, two-sided Wilcoxon signed-rank test; Fig. 3*C*) (53–55). In addition, we assessed the group-level power spectral density (PSD) of both groups of pHFOs and nHFOs by measuring the full width at half maximum of the PSD peak, which represents the frequency range where spectral power exceeds half of its peak. Overall, pHFOs comprised a notably smaller spectral range of power augmentation than nHFOs (pHFOs: 61.4 ± 42.6 Hz, nHFOs: 86.8 ± 46.6 Hz, mean ± SD; $n = 25$; $P = 0.0137$, $d = 0.56$, two-sided Mann–Whitney U test; Fig. 3 *B* and *C*), suggesting that pHFOs are more narrow banded (44).

Furthermore, we explored the cross-frequency relationship (51, 56) between the low (4 to 30 Hz, peri-ripple band associated with interictal spikes) and high (>80 Hz, ripple band) frequency bands (*SI Appendix*, Text S3). First, we measured the time of occurrence for p/nHFO relative to the spike peak, showing that the pHFOs were highly concentrated prior to the spike peak, while nHFOs were more uniformly distributed (*SI Appendix*, Fig. S4*A*). Furthermore, we examined the riding phase of the HFO events on the peri-ripple signal. In Fig. 3*A*, the examples illustrated that a typical pHFO appears before the peak of the peri-ripple signal, while nHFOs tend to distribute widely around the peak. Group-level analysis showed clear nonuniform phase distributions present for both groups ($n = 229$ pHFOs, $n = 1{,}248$ nHFOs; both $P < 10^{-4}$, Rayleigh test for circular nonuniformity), indicating strong preferred phase on the low-frequency activity. However, the mean phase differed significantly (pHFOs: [−33.2°, − 13.0°], 95% CI, compared to nHFOs: [−3.2°, 13.7°]; $P < 10^{-4}$, $d = 20$, Kruskal–Wallis equivalent test for circular population; Fig. 3*D*), which suggests that the activity of pHFOs are coupled with the rising flank of the peri-ripple signal, while nHFOs are more aligned at the peak.

Categorization of HFO-Informed Spikes. The next question we asked was whether those interictal spikes associating with different groups of HFOs (i.e., p/nHFOs) present distinct and concordant characteristics as well. According to the grouping of HFOs, the spike population of each patient was categorized into three groups, namely, pSpikes (spikes with pHFOs, 9.4 ± 11.6%, mean ± SD, $n = 25$), nSpikes (spikes with nHFOs, 30.0 ± 14.2%), and rSpikes (the remaining spikes without any form of concurrent detections, 60.6 ± 19.3%; Figs. 1*A* and 4*A*), which is consistent with the previous noninvasive studies (12, 39, 57). Furthermore, in patients who had SOZ information available ($n = 8$, *SI Appendix*, Table S1), we found higher, but unremarkable, percent of pSpikes in the patients with lateral onsets (8.44 ± 7.93%, $n = 3$) compared to the patients involving mesial onsets (5.98 ± 1.84%, $n = 5$, $P = 0.79$, two-sided Mann–Whitney U test).

Across all patients, we found a significant difference in the amplitude of the spikes (defined as the relative voltage between the main peak and trough of a spike) (51) among groups ($n = 25$, $P < 10–4$, Kruskal–Wallis test). pSpikes especially had the highest amplitude compared to nSpikes ($n = 25$; $P = 0.0081$, $d = 0.63$, false discovery rate (FDR) corrected) and rSpikes ($P = 0.00029$, $d = 1.30$), and the amplitude of nSpikes was also higher than rSpikes ($P = 0.0081$, $d = 0.86$; Fig. 4 *B* and *D*). However, the width of the main peak yielded no remarkable difference among groups ($n = 25$; $P = 0.54$, Kruskal–Wallis test). Additionally, spectral analysis yielded a notable difference in the median frequency of spikes in the ripple band among groups ($n = 25$; $P = 0.016$, Friedman's test), which further indicated that pSpikes had the lowest median frequency compared to nSpikes ($P = 0.019$, $d = 0.32$, FDR corrected) and rSpikes ($P = 0.016$, $d = 0.37$), while no clear difference was found between n/rSpikes ($P = 0.48$, $d = 0.05$; Fig. 4 *B* and *D*). In addition, pSpikes had higher

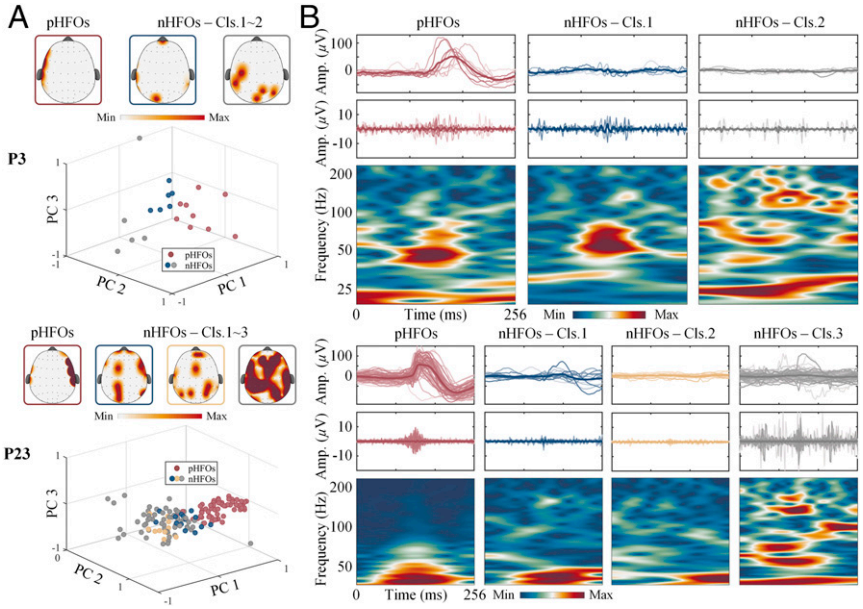

Fig. 2. Clustered HFOs in three-dimensional space and spatiotemporal profiles of p/nHFOs in two patients. (*A*) HFOs are clustered in the high-dimensional feature space and shown in the three largest principal component (PC) spaces, with pHFOs in red and other nHFO groups in blue/yellow/gray. Scalp distributions of channels, where events from each group are detected, are shown correspondingly. Note the spread/focality of the scalp map in each group. (*B*) HFO events in each group are displayed with raw data, the high-pass filtered (>80 Hz) data, and the time-frequency representations. The signal traces are piled with the mean in bold, and colors correspond to each group in *A*. Note that pHFOs are highly associated with the spike profile, while nHFOs are generally discordant with the spike either temporally or spatially; thus, spike traces are usually not visible in the nHFOs.

spectral heterogeneity [measured by the Kullback-Leibler divergence of the observed spectral distribution from the uniform distribution (58)] in the ripple band than nSpikes and rSpikes ($n = 25$; $P = 0.019$, $d = 0.82$ and $P = 0.040$, $d = 0.70$, respectively, Kruskal–Wallis test with FDR correction; Fig. 4 *B* and *D*), while the n/rSpikes were comparable ($P = 0.73$, $d = 0.08$), suggesting a

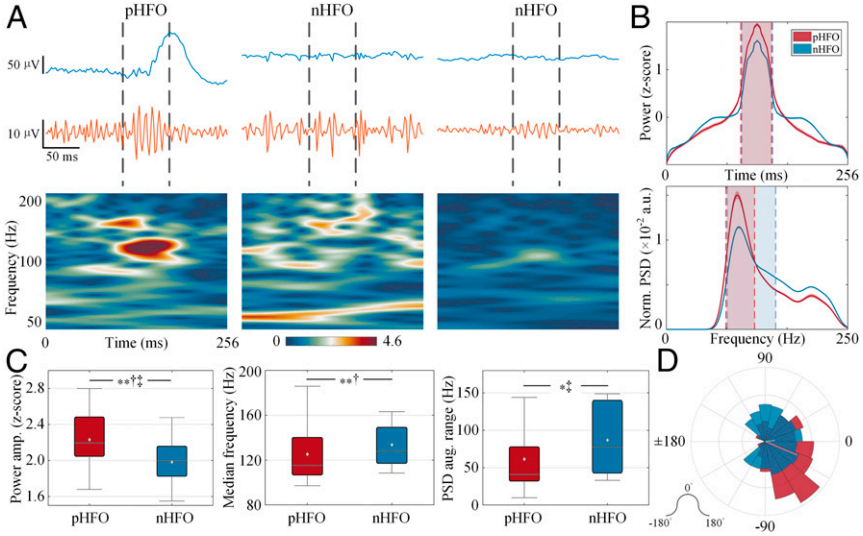

Fig. 3. Temporal and spectral characteristics of p/nHFOs. (*A*) Examples of p/nHFOs in P1 with raw signals in blue, high-pass filtered (>80 Hz) signals in orange, and time-frequency maps with power color coded. The interval where the HFA was detected is marked with dashed vertical lines. (*B*) Averaged power time course (*z*-scored) and averaged PSD (normalized by total spectral energy) in high-frequency band for p/nHFOs in all patients. The full width at half maximum is marked in dashed vertical lines with colored areas (pHFO in red and nHFO in blue). Note the elevated side lobes in nHFOs, while pHFOs are clearly discernable from the background. (*C*) Box plots of comparison in power peak, median frequency, and spectral width in all patients ($n = 25$). Note that pHFOs, in general, are events standing out from a flat background activity within a narrowband compared to nHFOs. The horizontal black line indicates the median, the light gray diamond denotes the mean, the vertical bars indicate the interquartile range (IQR), and the whiskers indicate the 1.5 IQR. (*D*) Riding phase of HFOs on the low-frequency signal (4 to 30 Hz, peri-ripple band) with the mean phase vector shown in a solid line ($n = 229$ pHFOs, $n = 1{,}248$ nHFOs). Note that both groups are nonuniformly distributed ($P < 10^{-4}$, Rayleigh test for circular nonuniformity); however, the pHFOs mainly distributed prior to the peak (0°) of the peri-ripple signal, while the nHFOs are averaged around the peak ($P < 10^{-4}$, $d = 0.20$, Kruskal–Wallis equivalent test for circular population). *$P < 0.05$, **$P < 0.01$, $^{\dagger}d > 0.2$, $^{\ddagger}d > 0.5$, and $^{\dagger\ddagger}d > 0.8$.

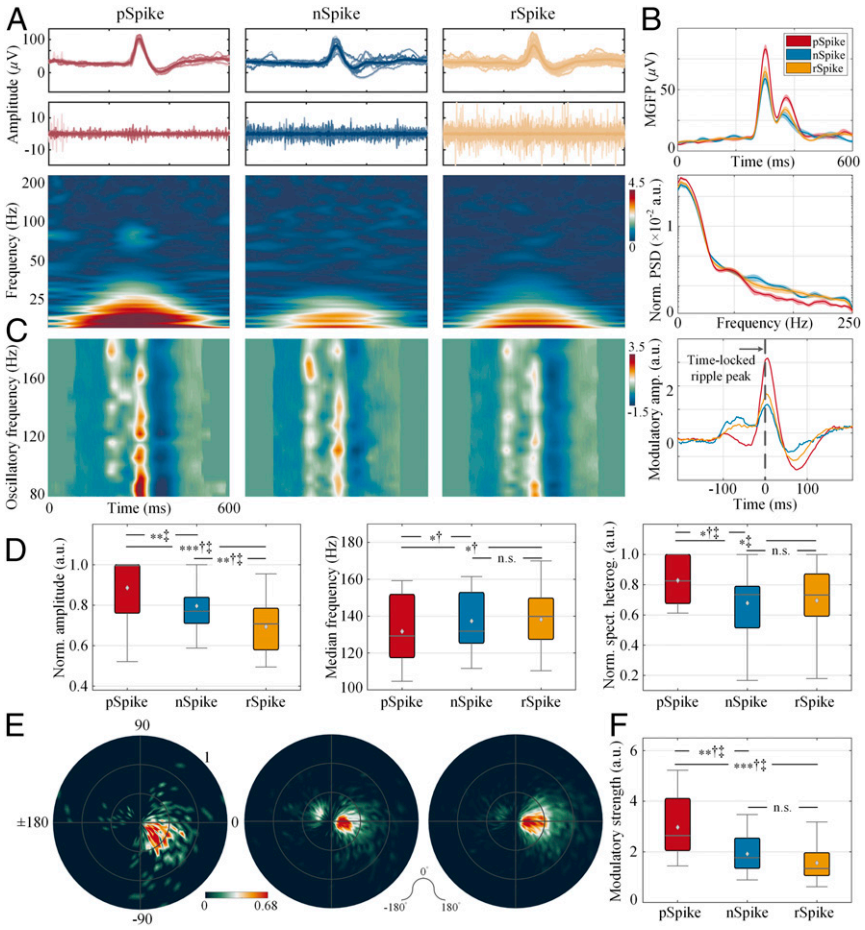

Fig. 4. Temporal and spectral characteristics of spikes categories—p/n/rSpikes. (*A*) Examples of spike groups in P3 with raw signals (*Top*), high-pass filtered (>80 Hz) signals (*Middle*), and time-frequency maps with power color coded (*Bottom*). The raw and filtered signal traces are piled, and the bold trace is the mean. (*B*) Averaged MGFP (mean global field power), broadband PSD, and averaged oscillation-triggered modulatory signal for p/n/rSpikes in P3. (*C*) Oscillation-triggered comodulograms (OTCG) for p/n/rSpikes in P3, representing the modulatory signals that are averaged at the peak of the narrowband oscillation for frequencies above 80 Hz. The color encodes the amplitude of the modulation. Note the strong modulation in the range from 80 to 120 Hz in pSpikes, while not in n/rSpikes. (*D*) Boxplot of group-level comparison for spike amplitude, median frequency in the ripple band, and spectral heterogeneity in all patients ($n = 25$). Note that pSpikes in general have higher amplitude and carry large spectral variability compared to n/rSpikes. The horizontal black line indicates the median, the light gray diamond denotes the mean, the vertical bars indicate the interquartile range (IQR), and the whiskers indicate the 1.5 IQR. (*E*) Ripple-phasor distributions of p/n/rSpikes ($n = 554$ pSpike phases, $n = 2{,}326$ nSpike phases, $n = 5{,}742$ rSpike phases), representing the coupling between spike phase and ripple amplitude, with color representing the density of ripple-phasor. The preferred phase of coupling in pSpikes is on the rising phase of the spike, prior to the peak of the spike, which is significantly different from that of n/rSpikes ($P < 10^{-4}$, $d = 0.53$ and 0.48, respectively, circular Kruskal–Wallis test with FDR correction), while the ripple-phasor of n/rSpikes comparably distributed around the peak of the spike ($P = 0.29$, $d = 0.18$). Note that the preferred phase of ripples on pSpikes is consistent with the riding phase of pHFOs. (*F*) Boxplot of modulatory strength for p/n/rSpikes across patients ($n = 25$). $^{*}P < 0.05$, $^{**}P < 0.01$, $^{***}P < 0.001$, $^{\dagger}d > 0.2$, $^{\ddagger}d > 0.5$, $^{\dagger\ddagger}d > 0.8$, and n.s. indicates not significant.

more uniform distribution of spectral energy above 80 Hz in n/rSpikes compared with pSpikes in which the energy is less distributed (Fig. 4 *A* and *B*).

Next, we examined the hypothesis that pSpikes have the most prominent cross-frequency coupling (CFC) compared to the other two groups (*SI Appendix*, Text S3). First, we assessed the phase locking between the low- and high-frequency activities in spikes by constructing ripple phasor (55), which describes the distribution of phase angles in the peri-ripple band corresponding to the occurrence of a ripple activity when associated with an epileptiform spike (Fig. 4E). The preferred phase of coupling in nSpikes and rSpikes was similarly toward the peak of the spike ($n = 2{,}326$ nSpike phases, $n = 5{,}742$ rSpike phases; $P = 0.29$, $d = 0.18$, circular Kruskal–Wallis test with FDR correction), whereas pSpikes ($n = 554$ pSpike phases) were significantly aligned at the negative phase before the peak of the spike comparing to nSpikes ($P < 10^{-4}$, $d = 0.53$) and rSpikes ($P < 10^{-4}$, $d = 0.48$). Next, to verify the strength of coupling indicated by the ripple phasor analysis, we performed the oscillation-triggered coupling analysis (55, 59) to compute the modulatory signal and the corresponding modulation strength. First, we found that the time of occurrence for prominent ripple band activities was relatively concentrated before the spike peak time in pSpikes while more uniformly distributed along the n/rSpike signals (*SI Appendix*, Fig. S4*B*), which is also aligned with the results of ripple phasor analysis. Furthermore, in Fig. 4*C*, we gave examples of oscillation-triggered comodulograms for p/n/rSpikes in P3, showing clear modulation in pSpikes of the peri-ripple activity with ripple band from 80 to 100 Hz in comparison with n/rSpikes. Further group-level analysis revealed significant difference in modulatory strength ($n = 25$; $P < 10^{-4}$, Kruskal–Wallis test; Fig. 4 *B* and *F*), where pSpikes had remarkably higher modulation strength than nSpikes ($P = 0.0019$, $d = 1.04$, FDR corrected) and rSpikes ($P < 10^{-4}$, $d = 1.39$); in contrast, no notable difference was found between n/rSpikes ($P = 0.06$, $d = 0.45$).

These results indicate that strong and consistent CFC are present between HFO and spike in pSpike signals.

Imaging Performance of pHFOs Compared to Conventional Spike Imaging. Given the morphological distinctions of the pHFOs (events of putative pathology) from the other HFA detections, we asked whether these identified pHFOs reveal and image the underlying EZ and, if so, how accurate they are compared to the conventional spike imaging method (60). To this end, we first extracted the multichannel EEG data of pHFO activities for each patient using a linear decomposition method on the basis of spatiospectral information of the oscillatory signal with a characteristic "peaky" spectral profile to optimize the signal-to-noise ratio (SNR) of the extracted activity (61, 62). Then, the electrical activity on the cortex was estimated from the extracted EEG data via ESI techniques to localize the underlying sources of the corresponding scalp-recorded pHFO activity (41, 63, 64). For spike imaging, the multichannel spike epochs identified in each patient were averaged to enhance the SNR of the spike activity and projected onto the cortex using the same source imaging method (60). The estimated EZs of both pHFOs and averaged spikes were compared to the clinical evidence—surgical resection ($n = 26$) and/or intracranial electrodes denoted as SOZ ($n = 11$) by epileptologists (Fig. 5*A*)—to evaluate the performance of the two imaging modalities in terms of localization error, normalized overlap ratio, and spatial dispersion for each patient (42, 64–67). Clinically, the true EZ can be approximated by the surgical resection in patients who become seizure free postsurgically (2); however, since the surgical resection is often conducted large enough to ensure that all epileptogenic tissue is removed, taking surgical area as EZ would most probably be an overestimate. Details about source imaging are reported in *Materials and Methods* and *SI Appendix*, Texts S4 and S5.

By estimating the current density distribution over the cortex using pHFOs and spikes, overall, the estimated EZ of pHFOs demonstrated constricted spatial activation, while spikes tended to have more spreading distributions (two examples depicted in Fig. 5*A* validated with resection area and SOZ, respectively). In the 24 patients with resection information available, 18 of them became seizure free; therefore, in these patients, the resection volume was used as an approximate of the true EZ. In this cohort, we found that the localization error to resection was remarkably lower in pHFOs compared to spike imaging ($n = 18$, pHFOs: 3.52 ± 1.42 mm, mean ± SD, compared to spikes: 9.57 ± 5.29 mm; $P = 0.0002$, $d = 1.53$, two-sided Wilcoxon signed-rank test; Fig. 5B), displaying a 162% (~5.36 mm) improvement. Additionally, in eight patients with SOZ labeled, the localization error between the estimated EZ and the SOZ was 10.05 ± 7.10 mm for pHFOs compared to 18.50 ± 6.41 mm for spikes, indicating a significant reduction of 186% (~12.48 mm) ($P = 0.0078$, $d = 1.18$, two-sided Wilcoxon signed-rank test; Fig. 5*C*). In addition, we found similar results in patients with ETLE (*SI Appendix*, Fig. S6 *B* and *C*).

Subsequently, in order to assess the spatial concordance of the imaging results to the clinical evidence, we adopted two other metrics, normalized overlap ratio and spatial dispersion (65–67), evaluating the spatial distribution of the estimated EZ based on the spread of resection area or SOZ (*SI Appendix*, Text S5). We first examined the precision of overlap between the estimated EZ and resection and found that the concordance is significantly higher in pHFOs ($n = 18$, 76 ± 23%, mean ± SD) than spikes (38 ± 17%; $P = 0.0002$, $d = 1.80$, two-sided Wilcoxon signed-rank test; Fig. 5*B*). Meanwhile, pHFOs had a conversely lower recall of overlap with the resection (77 ± 20%) compared to spikes (90 ± 15%; $P = 0.013$, $d = 0.75$, two-sided Wilcoxon signed-rank test; Fig. 5*B*). Likewise, we found a similar trend in the precision of overlap on the basis of SOZ, showing a notably higher precision using pHFOs than spikes ($n = 8$; $P = 0.023$, $d = 0.97$, two-sided Wilcoxon signed-rank test); however, the recall with SOZ was comparable in these two modalities, though the mean recall in pHFOs was slightly higher than that in spikes ($P > 0.5$, $d = 0.13$, two-sided Wilcoxon signed-rank test; Fig. 5*C*). These results indicate that the estimated EZ of pHFOs is spatially more focal and specific, while spikes are often widespread over areas beyond the EZ. By combining the precision and recall in the sense of geometric mean (or simply normalized overlap ratio), which represents the overall concordance between the estimation and the ground truth, we found higher normalized overlap ratio in pHFOs compared to spike imaging when validated by resection ($n = 18$; $P = 0.00028$, $d = 1.31$, two-sided Wilcoxon signed-rank test; Fig. 5*B*) and SOZ ($n = 8$; $P = 0.039$, $d = 0.92$, two-sided Wilcoxon signed-rank test; Fig. 5*C*). Furthermore, the measurement of spatial dispersion strongly affirmed our findings in overlap ratio, which shows significantly smaller spreading in pHFOs than spikes, validated based on both resection ($n = 18$; $P = 0.0002$, $d = 1.94$, two-sided Wilcoxon signed-rank test; Fig. 5*B*) and SOZ ($n = 8$; $P = 0.0078$, $d = 1.13$, two-sided Wilcoxon signed-rank test; Fig. 5*C*). Moreover, we observed concordant results in patients with ETLE (*SI Appendix*, Fig. S6 *B* and *C*). Additionally, we examined the imaging performance in patients with deep foci (mesial temporal onsets, $n = 5$, *SI Appendix*, Table S1) and found that the pHFOs were consistently better in localizing the SOZ than spikes (*SI Appendix*, Fig. S9). These results suggest that pHFOs in general are more spatially concordant with the clinically defined EZ, in contrast to spikes which are spatially more spread.

Association of Estimated EZ with Surgical Outcomes. Once we evaluated the imaging performance of the two modalities—pHFOs and spikes—in the seizure-free cohort, we sought to investigate two main questions. The first was whether the estimated EZ of these biomarkers is concordant with the resection area in non–seizure-free patients. The second was to inspect the relation between imaging performance and surgical outcomes (i.e., seizure free or non–seizure free). To answer the first question, we conducted the same imaging procedure as before in a cohort of six non–seizure-free patients with surgical information and calculated the corresponding imaging performance in terms of localization error, normalized overlap ratio, and spatial dispersion. By comparing these metrics between the seizure-free and non–seizure-free groups for pHFOs, we found dramatic degradation of localization error in the non–seizure-free group ($n = 6$, 9.19 ± 4.81 mm, mean ± SD) compared to the seizure-free group ($n = 18$, 3.52 ± 1.42 mm; $P = 0.00097$, $d = 2.10$, two-sided Mann–Whitney U test; Fig. 5*D*). Moreover, the normalized overlap ratio was significantly declined from 74 ± 11% ($n = 18$) in the seizure-free group to 53 ± 18% ($n = 6$) for the non–seizure-free group ($P = 0.0085$, $d = 1.54$, two-sided Mann–Whitney U test; Fig. 5*D*), and the comparison of spatial dispersion was consistent, giving an over 215% increment in the non–seizure-free cohort compared with the seizure-free cohort ($P = 0.015$, $d = 1.56$, two-sided Mann–Whitney U test; Fig. 5*D*), indicating more spatial discordance between the estimated EZ and the surgical resection in the non–seizure-free group. In contrast, the metrics for spike imaging were not discriminable for surgical outcomes ($P > 0.5$, $d = 0.22$ to ~0.52, two-sided Mann–Whitney U test), though a weak degradation was observed in the non–seizure-free cohort (Fig. 5*D*).

Furthermore, we examined the association of imaging performance (based on resection) to the corresponding surgical outcomes for pHFO imaging. To do so, we constructed a generalized linear model (GLM) with a binomial distribution for the response variable, which is the surgical outcomes (i.e., seizure free or non–seizure free), and a linear predictor of measures in imaging performance (i.e., localization error, normalized overlap ratio, and spatial dispersion) via a logistic link function (68). Given that the source imaging results were consistent across the TLE and ETLE cohorts, we therefore combined all patients for GLM analysis, including 20 seizure-free patients and 6 non–seizure-free patients. In these patients, all three measures yielded significant

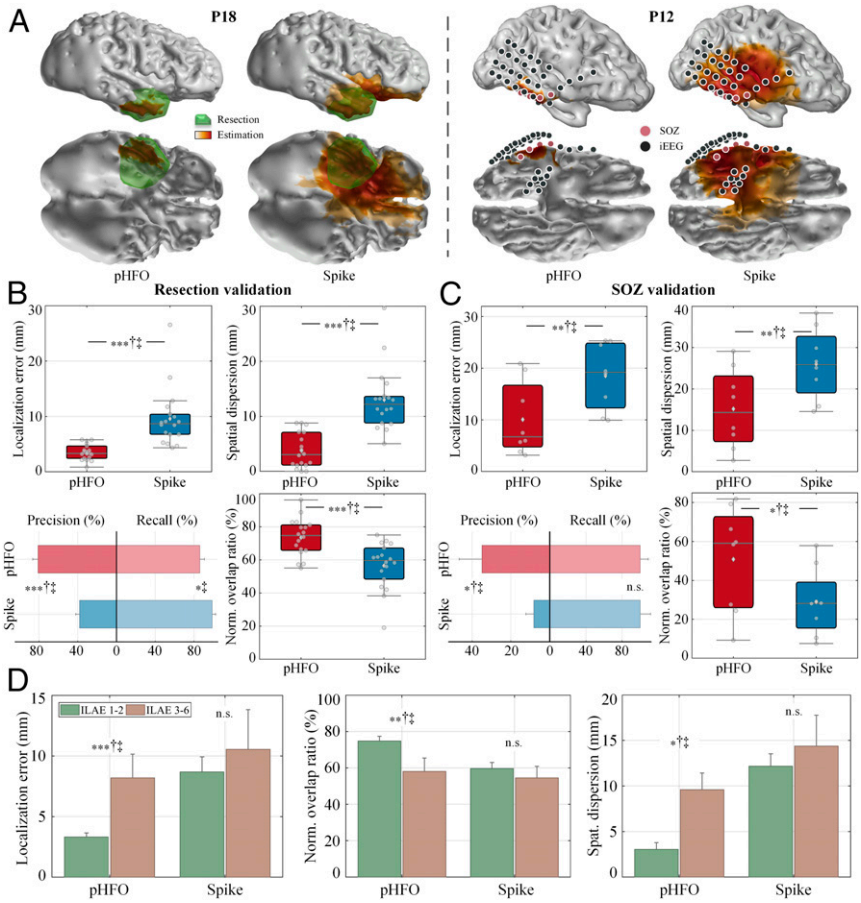

Fig. 5. Source imaging of pHFOs and spikes and association with clinical outcomes. (*A*) Examples of estimated EZ (color coded in strength of source activation) on the individual cortex model (derived from preoperational MRI) in P18 and P12 with validation against resection area (green) or SOZ (pink) labeled from intracranial EEG electrodes (black). (*B*) Imaging performance metrics measuring localization error, spatial overlap normalized by either estimated EZ (precision) or resection (recall), geometric mean of precision and recall, and spatial dispersion in a cohort of seizure-free (SF) patients with resection information available ($n = 18$). Note that the conventional spike imaging gives concordant but overestimated results, while the estimation of pHFOs has higher concordance and specificity. Each gray circle corresponds to individual patient's data. The horizontal black line indicates the median, the light gray diamond denotes the mean, the vertical bars indicate the interquartile range (IQR), and the whiskers indicate the 1.5 IQR. In the bar graphs, the height denotes the median and the error bar indicates the SEM. (*C*) Imaging performance validated by SOZ in patients who had intracranial information ($n = 8$). (*D*) Comparison of imaging performance between SF ($n = 18$) and nonseizure-free (NSF) ($n = 6$) patients for pHFOs and spike in comparison to surgical resection. There is a clear degradation of imaging performance from SF to NSF cohort in pHFO imaging but no significant difference in spike imaging. $^{*}P < 0.05$, $^{**}P < 0.01$, $^{***}P < 0.001$, $^{\dagger}d > 0.2$, $^{\ddagger}d > 0.5$, $^{\dagger\ddagger}d > 0.8$, and n.s. indicates not significant.

predictors of the surgical outcomes ($P < 0.01$, χ^2 test; *SI Appendix*, Fig. S5), among which the localization error was found to be the optimal predictor ($P < 10^{-4}$, χ^2 test) with an odds ratio of 3.8 (95% CI: 1.07 to 13.53) for the non–seizure-free outcome per unit (1 mm) increase in localization error (*SI Appendix*, Fig. S5). These findings suggest that an inverse relationship exists between the imaging performance measures—from the estimated EZ to the surgical resection—and the clinical outcomes; in other words, the more spatially concordant the imaging results for pHFOs are, the higher the probability of seizure freedom in patients.

Improved Imaging Performance of HFO-Informed Spikes. The observation that spikes are separable by the co-occurrence of HFOs into p/n/rSpike categories which demonstrated notable differences in morphology raised the question of whether the presence of HFOs on the spikes leads to high concordance to the underlying epileptogenicity or, alternatively, whether pSpikes provide better localization of the true EZ compared to the other two groups. To address this, we used a randomized spike imaging test based on bootstrapping to control the number of spikes averaged in the imaging process for fair comparison among groups (*Materials and Methods*). In the seizure-free patients who had resection information available ($n = 18$), by comparing the imaging performance among groups of spikes, we found significant difference in the metrics of localization error ($P = 0.045$, Kruskal–Wallis test; Fig. 6 *A* and *B*). More specifically, pSpikes achieved significantly lower localization error compared to nSpikes and rSpikes ($n = 18$, $P < 0.05$, $d = 0.41$, FDR corrected), while no difference was found between nSpikes and rSpikes ($P > 0.5$, $d = 0.02$). Although there was no remarkable difference in the measures of normalized overlap ratio and spatial dispersion, the overall trends were consistent with the localization error, showing a better performance in pSpikes compared to n/rSpikes ($n = 18$, $P = 0.056$ to $\sim$0.079, $d =$ 0.40 to $\sim$0.42, FDR corrected). Moreover, weak but not notable imaging improvement was observed for pSpikes in the cohort of patients in whom the SOZ was used for validation ($n = 8$, $P > 0.05$, Kruskal–Wallis test; *SI Appendix*, Fig. S7*A*).

The notion of "red" and "green" spikes has been proposed in the literature, referring to those more likely to correlate with epileptogenicity and those not (45). Later studies confirmed that spikes might be separable in their capability of indicating the actual or latent EZ (69). Therefore, given that collected spikes could come from bilateral or multiple foci in some patients, we asked whether the co-occurrence with pHFOs leads to better

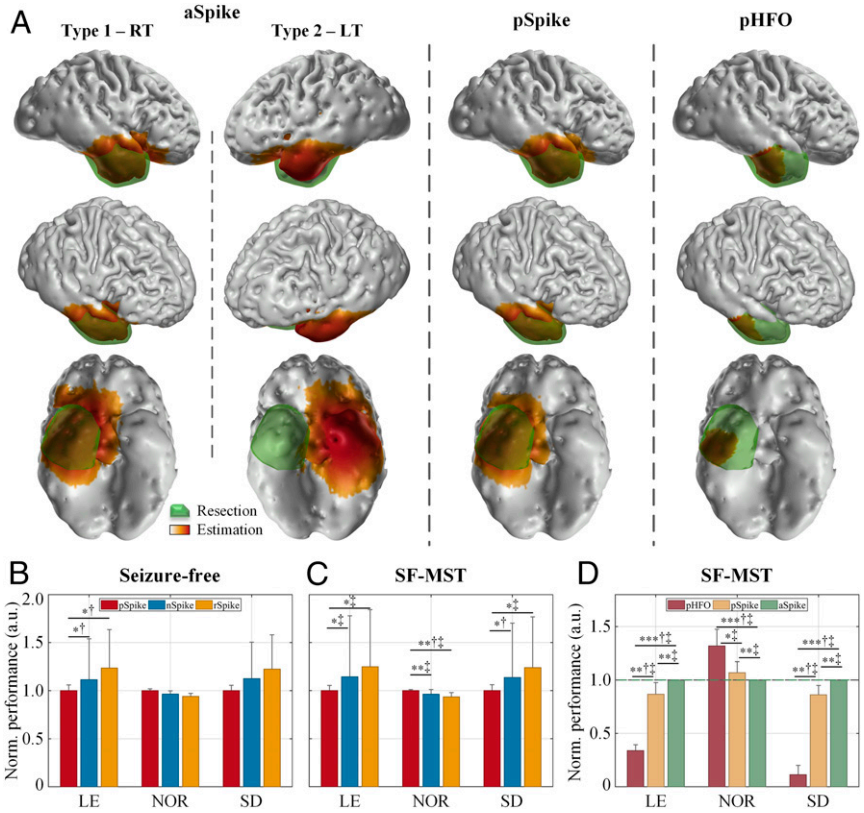

Fig. 6. Improved source imaging performance of HFO-informed spikes—pSpikes. (*A*) Examples of estimated EZ for conventional spike imaging, pSpike imaging, and pHFO imaging in P17. In this case, interictal spikes have bilateral origins, so the conventional spike imaging captures both sides, while pSpike and pHFO imaging selectively colocalizes to the right temporal area. (*B*) Imaging performance of pSpikes in seizure-free (SF) cohort with resection validation (n = 18). In the bar graphs, the height denotes the median and the error bar indicates the SEM. (*C*) Imaging performance of pSpikes in a cohort of 12 patients with MST. Note that imaging performance is further boosted in this cohort with MST, suggesting the co-occurrence of HFOs on spikes as a discriminator of spikes with higher epileptic significance. (*D*) Comparison of imaging performance among pHFOs, pSpikes, and conventional spike imaging (aSpikes) as baseline (green dashed line) in the cohort of SF-MST patients (n = 12). RT = right temporal, LT = left temporal, SF = seizure-free. $^{*}P < 0.05$, $^{**}P < 0.01$, $^{***}P < 0.001$, $^{\dagger}d > 0.2$, $^{\ddagger}d > 0.5$, and $^{\dagger\ddagger}d > 0.8$.

selection of those "red" spikes highly correlated with the true EZ. From the previous analysis, we found that 80% of patients in which pSpikes outperformed n/rSpikes in localization error had MST and, likewise, around 91% in normalized overlap ratio and 80% in spatial dispersion. Therefore, we compared the imaging performance of p/n/rSpikes in subcohorts of patients with MST (n = 12) or single spike type (SST, n = 6). Interestingly, we discovered remarkably better concordance in pSpike imaging in the MST cohort compared to the other two groups in all performance metrics (n = 12, P = 0.0011 to ~0.0275, d = 0.48 to ~0.85, Kruskal–Wallis test with FDR correction; Fig. 6*C*). In contrast, the imaging results in SST patients were comparable among spike groups (n = 6, $P > 0.1$, Kruskal–Wallis test; *SI Appendix*, Fig. S7*B*). Hence, these results indicate that the spikes co-occurring with pHFOs (pSpikes) better indicate the underlying epileptogenicity and can be used as a criterion to objectively select more epileptically relevant spike type(s) out of multiple available spike types. In addition, we explored the association of the concordance in pSpike imaging (to the resection) with the surgical outcomes; however, none of the imaging metrics of pSpikes gave a notable fitting for the GLM (n = 24, $P > 0.05$, χ^2 test).

Last, we asked whether pHFOs or pSpikes are more effective biomarkers in localizing the underlying EZ. For this, we normalized the imaging results of the two modalities to those achieved by the conventional spike imaging (aSpikes) as a baseline for comparison. In the seizure-free patients who had MST, we found significant differences among the three imaging modalities (i.e., pHFOs, pSpikes, and aSpikes) in all performance metrics (n = 12, $P <$ 0.0005, Kruskal–Wallis test; Fig. 6*D*). In detail, pSpikes produced lower localization error than aSpikes, as validated by the surgical resection (P = 0.0034, d = 0.51, FDR corrected); meanwhile, the localization error was further reduced in pHFO imaging compared to pSpikes (P = 0.0034, d = 1.38) and aSpikes ($P < 10^{-4}$, d = 4.11). Additionally, similar trends were found in the performance of normalized overlap ratio and spatial dispersion, where pSpikes and pHFOs both depicted higher overlap ratio and lower spatial dispersion compared to aSpikes (n =12, $P < 0.01$, d = 0.56 to ~3.34, Kruskal–Wallis test with FDR correction); furthermore, pHFOs outperformed pSpikes in both normalized overlap ratio (P = 0.04, d = 0.52) and spatial dispersion (P = 0.002, d = 1.81, Fig. 6*D*). Likewise, we compared the source imaging results of pHFOs and pSpikes in the patients who had SOZ identified (n = 8) and found consistent findings that pHFOs in general are better localized to the presumed EZ compared to pSpikes (*SI Appendix*, Fig. S7*C*).

Discussion

This study aimed to establish a tractable means using noninvasive HFOs for accurate localization of focal epileptogenic tissue and delineation of the underlying epileptogenicity based on the hypothesis that the co-occurrence of HFOs and spikes with repetitive patterns provides a robust signature to discriminate pathological HFOs and delineate the underlying EZ in noninvasive EEG recordings, which, in turn, demarks the spikes of higher epileptic significance compared to the general spike population. The research objectives were addressed by 1) developing a

noninvasive and automatic approach to identify HFOs riding on spikes in scalp EEGs of patients with medically refractory epilepsy, 2) investigating the characteristics of HFOs and spikes in the presence or absence of the co-occurrence status, and 3) demonstrating the utility of the identified HFOs in delineating the cortical regions of epileptic abnormality validated by clinical evidence of surgical resection and SOZ.

Together, our results can be summarized as follows. First, we identified a subtype of HFOs concurrent with epileptiform spikes as a potential epileptic biomarker which is easy to observe and discriminate in noisy scalp EEG recordings. Second, we found that these pHFOs are distinctive from the nHFOs (events without consistency on spikes) in various temporal, spectral, and CFC patterns across patients. Moreover, similar discriminability was observed in diverse morphological characteristics among the subgroups of spikes (i.e., pSpikes, nSpikes, and rSpikes), corresponding to the presence of p/nHFOs. Third, our findings in source analysis revealed that the identified pHFOs are highly concordant to the EZ defined by the clinical resection and the SOZ in the cortical source domain compared to conventional spike imaging. In addition, we demonstrated that the congruence between the surgical resection and the pHFO sources is correlated with the surgical outcomes. Furthermore, we learned that the concurrence between HFOs and spikes not only identifies a subtype of epileptic HFOs but also selects a spike subgroup, which in turn outperforms the subgroups of spike imaging, suggesting that pHFOs can serve as a discriminator for identifying "red" spikes that are of high significance to determine the EZ.

Previous studies have proposed computational methods toward the detection of HFOs in scalp recordings (32, 38–40); however, such semiautomated approaches rely heavily on visual inspection to ensure optimal performance, and the successful discrimination of pathological from nonepileptic activates is still challenging and hinders the clinical utility. In the present study, we introduced an approach for automatic identification of putative HFOs combining an established architecture consisting of detection and discrimination components in invasive studies (70, 71) and discriminative features tailored to tackle the challenging conditions in scalp recordings based on two premises—concurrence with interictal spikes (7, 11, 46) and repetitive patterns (43)—to assist with the identification of epileptic activities. The proposed method was shown to outperform a well-established benchmark detector (39) in various simulation scenarios, which is attributed to the integration of high sensitivity detection and unsupervised learning techniques; however, due to the intrinsic differences and design strategy (e.g., semiautomated versus automated approach), direct comparison might be difficult and future investigation in both large-scale simulation and clinical study in comparing these detection approaches would be necessary. Also note that the present approach is independent of the spike detection procedure and operates on both segmented spike epochs and continuous recordings. In this study, spike epochs were collected, using Persyst and expert review, to investigate the characteristics of spikes with and without the concurrent HFOs based on the hypothesis that the concurrence between HFOs and spikes reciprocally identifies activities of higher degree of epileptic significance.

Subsequently, we showed distinctive spatiotemporal difference of pHFOs coexisting with interictal spikes, also known as spike ripples in previous studies (32, 39), from other HFAs without such concurrent patterns (nHFOs). Our results are aligned with previous studies showing pathological HFOs tend to have constrained distribution in the sensor level (50, 51) with regular and repetitive waveforms (43, 70), in contrast to the nHFOs which have widely distributed scalp topology and irregular shapes (43), from which we speculate that these nHFOs are a collection of HFAs originating from eloquent areas (21, 30, 43), biological (13, 21) and filtering artifacts (13, 22), or probably even independent epileptic HFOs (18, 44). Additionally, our study lends support to the published findings that epileptic HFOs are burst-like activities with clear separation from the background, while the nonepileptiform HFAs are broadband and embedded in oscillatory background without a clear-cut (44, 52, 54).

Cross-frequency interaction is of particular interest in epilepsy research (7), which might potentially distinguish pathological and physiological HFOs. Invasive studies have shown that the superimposed HFO on spike may indicate high association of epileptogenicity (30), with increased phase-amplitude coupling within SOZ (55). Our analysis is consistent with the previous findings by documenting strong modulation between low- and high-frequency bands in the pSpikes that are indexed by pHFOs compared to n/rSpikes. Furthermore, consistent phase locking was affirmed by pHFOs and pSpikes, indicating that putative HFOs tend to appear preferably prior to the peak of the spike signal coincidently on the rising phase, which is in line with the previous studies in both human and animal models (51, 72). Moreover, the preferred phase of coupling also suggests that pHFOs are unlikely to result from filtering spikes (51), unlike n/rSpikes, because artifactual events generated by ringing effect are often centered at the peak of sharp waves (22).

We found that pHFOs in the cortical source domain are highly concordant with the clinical evidence modeled by the surgical resection and SOZ, surpassing the conventional spike imaging method, which might owe to the spatial focality and selectivity of pHFOs (Fig. 2*A*), while spikes are less specific in general. This is consistent with the previous studies that note the specificity of HFOs to the epileptogenic area (12, 57) with a smaller extent than the IZ (73). We also observed the efficacy of pHFOs in localizing the SOZ even when deep foci were present, which might attribute partly to the capability of identifying HFOs in high-density EEG, which has been shown to allow better observability of the HFOs (74). Furthermore, in cases with mesial temporal onsets, we found that the occurrence and amplitude of pHFOs was relatively lower than the lateral onset cases (statistically not significant), whereas the pHFOs could still be stably identified from the scalp EEG. Therefore, the present approach could be potentially translated to cases where stereo-electroencephalography (SEEG) is used and the SOZ involves deep sources, especially when visual inspection of HFOs is excessively difficult in high-density EEG. Furthermore, given that the spatial sampling of SEEG is relatively limited (6), our approach to study the scalp-recorded pHFOs would be a good complement to SEEG investigations. However, since pHFOs could be less observable in cases with deep sources and the intracranial investigation of the studied cohort is limited to subdural grids and depth electrodes, future research in patients with SEEG involving superficial and deep onsets is necessary to further evaluate the proposed approach.

Several research groups have been exploring the possibility of localizing HFO sources from scalp EEG/MEG recordings (75–77); however, these studies have not fully addressed two issues: first, there lacks an objective means to distinguish pathological from physiological and artifactual HFAs (12, 78); second, the practicality and translational efficacy of such approaches is further hindered by manual review of HFOs in isolated short data segments (29). Our present work built a link between the automatic identification and source imaging of epileptic HFOs with a tractable means to study and delineate pathological generators in epilepsy patients from the scalp. In addition, we surprisingly found that the pSpikes selected by pHFOs in turn demonstrated distinctive morphological properties (51, 55) and elevated specificity in localizing the EZ compared to the other spikes without pHFOs. Further analysis also depicted that pHFOs are superior to pSpikes in localization performance. These findings in spike analysis might suggest a potential pathological meaning of the concurrence between the HFOs and spikes, which implies that the identified pHFOs are of epileptic significance. This bidirectional evidence might indicate the selectivity of pHFOs in separating "red" spikes (18, 30, 45) and

suggests a possible mechanistic network of mutual pathology underlying co-occurrence of HFOs and spikes.

It is commonly accepted that HFOs and spikes might represent similar neuronal networks but independent neurophysiological mechanisms (7, 18). Accordingly, spikes are considered as summated postsynaptic potentials from hyperexcitable and hypersynchronous pyramidal cells, but disrupted connectivity could lead out-of-phase firing and produce HFOs (23, 79, 80), which might result from neural loss (81) or altered GABAergic interneuron inhibition (82, 83). Moreover, HFOs tend to behave more similar to seizures than spikes (84); therefore, the concurrence of HFOs with spikes could potentially index the critical brain area of highly pathological nature, which might contribute to the high specificity of pHFOs to epileptic zones and the selectivity of pSpikes. Furthermore, recent advances suggested that epileptic tissue is transiently impaired instead of fully dysfunctional (44) and that the activation of HFOs is correlated differently with the postspike inhibition across ictogenesis (14, 85, 86). Therefore, we speculate that the transient impairment of epileptic tissue presents varying pathophysiological status, leading to different levels of network disruption, thus possibly explaining the distinct presence of coupling between HFOs and spikes within the same epileptic foci. There is also evidence that the alternation of excitation–inhibition balance in the epileptic network has relevance for the development of interictal activities and evolvement into seizures (87, 88). Therefore, the concurrent HFOs and spikes might share a mutual underlying pathological relationship and could reciprocally serve as a crucially important signature of epileptic status and therapeutic progress.

In this study, we provide a systematic and tractable approach to study pathological HFOs in scalp recordings for the delineation of underlying EZ. Our results also suggest potential means to examine artifactual HFOs, such as by phase-coupling measures. Moreover, we provide evidence that the reciprocal concurrence of pHFOs potentially selects the "red" spikes with high pathophysiological relevance from general spike populations, which helps delineate subareas of the IZ. This could be important in understanding the structure or formation of the epileptic network and possibly leads to deeper insights of the evolution and role of the various epileptic biomarkers. Clinically, our findings have three potential implications. First, the identified pHFOs could reveal or lateralize the potential epileptic foci and demark the "red" spike subgroups, which can assist for presurgical planning or invasive investigation. Second, the source imaging analysis of pHFOs can provide estimation of the underlying EZ in individual patients with focal epilepsy, which could further facilitate in planning for surgical intervention, such as resection or neuromodulation, and provide evaluation of the treatment outcomes. Third, our results raise the possibility of accurately investigating epilepsy without having to record seizures, which is resource consuming and prone to induce additional risks of secondary generalization due to medication reduction or cessation for prolonged video-monitoring prior to neurosurgery (89). Together, our findings suggest that the utility of concurrent HFOs with spikes in scalp recordings is highly desirable, which might be a critical resource for clinical translation in numerous patients and extend the application from presurgical diagnosis to monitoring of disease severity, tracking therapeutic progress, and providing postsurgical evaluation in vulnerable patient populations.

This study was designed to objectively investigate pathological HFOs in scalp recordings for focal epilepsy, especially for TLE; however, this disease population may have facilitated the identification of HFOs and spikes, which consequently makes it useful to investigate other epilepsy types such as absence seizure, in which spike and wave is a marked characteristic (86) and ictal mechanisms and origins are still being investigated (90). Likewise, although we included four patients involving extratemporal foci as case studies and found highly consistent results in line with the TLE cohort, the sample size is barely enough to draw strong conclusions. Further studies in patients with ETLE would be needed to confirm the findings in this study. Furthermore, there also exist HFOs independent of spike but of pathological value (18, 44) that are not being detected with our approach. Although it is still unclear how such independent HFOs are to be distinguished from other HFAs, in the absence of discriminators such as epileptiform spikes, the exploration of these HFOs is an interesting topic for a future study. Moreover, research on the neurophysiological basis of the formation and evolution of HFOs and spikes and their relevant role in the epileptic network remains to be done. More importantly, clinical translation of scalp HFOs and their associated spikes in various applications is a crucial move to potentially improve clinical practice and hugely benefit patients with epilepsy.

Materials and Methods

Patient Population and Data Collection. In total, 25 patients (14 females, aged 19 to 60 y; *SI Appendix*, Table S1) with TLE and 4 patients with ETLE (two females, aged 21 to 47 y; *SI Appendix*, Table S2) were included in this study. All patients were recruited and evaluated by trained epileptologists at Mayo Clinic. The criteria of inclusion were as follows: 1) patients who underwent presurgical investigations, including high-density video EEG, high-resolution MRI, and neuropsychological assessment; 2) patients eligible for resective surgery and/or intracranial EEG monitoring; 3) patients whose scalp EEG recordings contained clear and frequent interictal spikes identified by the clinicians; and 4) patients who had at least 1 y of follow up with postsurgical evaluation and/or iEEG study available to define the resection and/or SOZ location. The main investigations were based on the temporal cohort, and the extratemporal patients were included as case studies.

All patients underwent long-term presurgical monitoring using a 76-channel EEG system (Xltek, Natus Medical Incorporated). Each electrode was glued over the scalp according to a 10-10 montage with the reference electrode at CPz. The EEG signals were recorded with a sampling rate of 500 Hz and high pass filtered above 1 Hz to remove spurious slow activity and DC drifts. The outcomes of surgical intervention were determined by the clinicians following the International League Against Epilepsy (ILAE) criteria (91) during the follow-up period (n = 29, 19 $\pm$ 6.8 mo, mean $\pm$ SD). Among all patients, 21 patients were scored as ILAE 1 to 2 (seizure free; 12 females), and 8 were scored ILAE 3 to 6 (non–seizure free; 4 females). The study was approved by the Institutional Review Boards of Carnegie Mellon University and Mayo Clinic, and all patients gave informed consent to participate in this study.

Overview of HFO Detection and Discrimination. All identified spikes were extracted in the temporal window from −500 to +500 ms surrounding the predominant peak, and it was ensured that no obvious artifacts existed during this interval. In each patient, the extracted epochs were manually examined in Matlab (The MathWorks, Inc.) using EEGLab toolbox, and independent component analysis was conducted to eliminate common artifacts, such as eye blinks, which have distinct spatiotemporal features (i.e., high/sharp activity in the anterior electrodes). Then, all spike epochs were used for automatic detection of HFOs independently on each channel using our proposed approach, which is constructed based on a previously established structure, consisting of detection and discrimination components, in invasive studies (70, 71). The proposed method integrates the concurrence of interictal spikes (7, 11, 46) with repetitive patterns (43) of HFOs to disentangle pathological activities from other HFAs. For each patient, spike epochs were first filtered using a zero-phase finite impulse response (FIR) band-pass filter (64th order) from 80 to 240 Hz and screened by an energy detector to discover all possible candidates of HFAs distinguishable from the background. Specifically, in each channel, the distribution of SD for the signal amplitude was computed with a 100 ms moving window. Then, a baseline threshold was set at two times the median of the SD distribution, and all samples in the filtered signal with an absolute amplitude exceeding this level were stored as the initial detection of candidates. In general, a low baseline could warrant high sensitivity in this initial phase. Each of the detected candidates was extracted as a segment of 128 ms before and after its peak, within which the background envelope of the filtered epoch in the first and last 80 ms was calculated using Hilbert transform, and a baseline was set at two times the median of the envelope distribution. Then, the number of crossing relative to this baseline was counted for the central 80 ms for each detected event, and those with a crossing number exceeding eight (two per each of the four cycles) were sieved from the initial detections, which aligns with the clinical definition of typical HFOs (11,

13). Furthermore, the number of zero-crossing in the unfiltered signal was also counted, and those events with a zero-crossing over 10 were discarded as noisy activities (70).

To discriminate the putative HFOs with high precision, we designed a set of representative features, combining various temporal, spectral, and spectrogram measures, extracted from each of the survived events in both unfiltered and filtered (>80 Hz) data (*SI Appendix*, Text S1). Next, upon the extracted features, the detected events were separated into several clusters using Gaussian Mixture Model in an unsupervised manner, which was initialized by *k*-means clustering with the optimal number of clusters determined by the elbow method (92). The clusters of pHFOs were identified by the spatiotemporal association co-occurring with spikes. Specifically, once the clusters were formed, the activities within each cluster were displayed by the piled waveforms of unfiltered and filtered data as well as the spatial distribution of the channels where these events were detected, as shown in Fig. 2. The morphology of the unfiltered and filtered traces could easily distinguish the clustered putative pHFOs riding on spikes (pHFOs), and the repeatability of the clustered events could affirm whether these events occurred consistently or occasionally from the piled signals and their spatial distribution. Then, the remaining events not consistently co-occurring with spikes were labeled as nHFOs. A diagram of the adopted algorithm is provided in *SI Appendix*, Fig. S1. In addition, the proposed identification method was compared to a well-established benchmark detector (32, 39) using a Monte Carlo simulation as detailed in *SI Appendix*, Text S2 and Figs. S1 and S2.

Electrophysiological Source Imaging. Upon the identification of pHFOs, the multichannel EEG were filtered above 80 Hz and transferred into time-frequency spectrogram (TFS) using short-time Fourier transform. The power within each TFS map was examined to find the most prominent peak and its temporal and spectral ranges (93). The multichannel epochs of pHFOs were concatenated along the temporal dimension. Given the estimated information of the time and frequency ranges of the pHFOs, the spatio-spectral decomposition (SSD) method (61, 62) was used to decompose the original multichannel data into orthogonal temporal basis functions, which assemble the oscillatory activities at specified temporal and spectral range and are paired with topological scalp maps representing the spatial activation of the basis. By projecting the original signal domain onto the prominent basis (62), the denoised pHFO data were extracted out of the noisy EEG signals (*SI Appendix*, Text S4).

Subsequently, we estimated the cortical source distribution of the extracted EEG data to image the underlying activities of pHFOs via ESI techniques, which is the process of estimating cortical activity from scalp recordings using the electrophysiological properties and geometry of the head to counter the effects of volume conduction (41). Since many established methods can be used to solve this inverse projection problem (41), for simplicity and reproducibility, the standardized low-resolution brain electromagnetic tomography (63) was employed. For spike imaging, the spike epochs were first band-pass filtered from 1 to 35 Hz to extract the main spectral power representing the spike activity, and then the filtered epochs were averaged to denoise the signals. The same ESI procedure was applied on the averaged spikes to estimate the underlying sources generating spike activities. In patients with MST, individual ESI analysis was performed on each spike type, but the performance measures, that is, localization error, normalized overlap ratio, and spatial dispersion, were averaged across all spike types in each individual patient (*SI Appendix*, Text S5). The estimated cortical source distributions for both pHFOs and averaged spikes were thresholded above the level of background activities using Otsu's method (94, 95). Moreover, the receiver operating characteristic curve was used to examine the possible effect of varying thresholds on the evaluation of imaging performance between pHFOs and spikes (*SI Appendix*, Fig. S8).

Randomized Spike Imaging Analysis. We separately performed imaging analysis in each subgroup of spikes (i.e., p/n/rSpikes) for each patient to assess the relative concordance of each subgroup with the clinical evidence. Due to the fact that the number of spikes in each subgroup was mostly unequal, simple averaging within each group might result in varying SNR across subgroups, as noise level is generally inversely correlated with the number of spikes averaged, thus leading to a biased imaging evaluation and an unfair comparison. Therefore, to address this issue, we deployed a randomized imaging test based on bootstrapping. Basically, for each patient, we pooled and resampled the spikes within the two subgroups with a larger sample size to withdraw a certain number of spikes according to the size of the minimum subgroup. Across all patients, the average number of resampled spikes was about 6 ± 4 (mean $\pm$ SD), and the pooled size was about 34 ± 23. The ESI analysis was performed on the averaged spike epoch from every surrogate trial to estimate the current source density and compute imaging performance, which we call an observation. This procedure was repeated 1,000 times to generate a distribution of imaging observations in the subgroups with a larger size, while for the minimum subgroup, ESI was evaluated only once. For group-level comparison, the imaging performance was averaged across surrogate trials for each spike subgroup and normalized to the best performance across subgroups within each patient.

Statistical Analysis. Statistical details are provided in the *Results* and corresponding figure legends. Descriptive statistics are shown as mean $\pm$ SD or 95% CI, as indicated. Statistical significance was set for $P < 0.05$, and the effect size was quantified using Cohen's d. All Statistical analysis and visualization were conducted in Matlab.

Data Availability. The analysis codes with sample data are available at GitHub, https://github.com/bfinl/HFOs-Identification-Imaging. The developed scripts and codes were written and tested using Matlab 2018a. We employed Curry 7 (Compumedics) and the EEGLab toolbox (version 13.6.5b) for visualization and preprocessing analyses (https://sccn.ucsd.edu/eeglab/index.php), as well as Persyst 13 for automated spike detection. Additionally, some open source Matlab plugins were used for signal processing and statistical analysis purposes, including the SSD toolbox (61) (https://github.com/svendaehne/matlab_SSD), the FDR toolbox (https://www.mathworks.com/matlabcentral/fileexchange/27418-fdr_bh), the MES toolbox (96) (https://www.mathworks.com/matlabcentral/fileexchange/32398-hhentschke-measures-of-effect-size-toolbox), and the CircStat toolbox (97) (https://www.mathworks.com/matlabcentral/fileexchange/10676-circular-statistics-toolbox-directional-statistics).

ACKNOWLEDGMENTS. This work was supported in part by NIH grants R01 NS096761, EB021027, MH114233, AT009263, and EB029354. We gratefully acknowledge all patients involved in the study and thank Rui Sun and Daniel Suma for discussions and help during data analysis and preparation of the manuscript. We thank Dr. Hari Guragain and Fan Yang for assistance in data preparation and Cindy Nelson in data collection.

1. R. D. Thijs, R. Surges, T. J. O'Brien, J. W. Sander, Epilepsy in adults. *Lancet* **393**, 689–701 (2019).
2. F. Rosenow, H. Lüders, Presurgical evaluation of epilepsy. *Brain* **124**, 1683–1700 (2001).
3. R. Kuzniecky, O. Devinsky, Surgery insight: Surgical management of epilepsy. *Nat. Clin. Pract. Neurol.* **3**, 673–681 (2007).
4. K. Malmgren, A. Edelvik, Long-term outcomes of surgical treatment for epilepsy in adults with regard to seizures, antiepileptic drug treatment and employment. *Seizure* **44**, 217–224 (2017).
5. R. Arya *et al*., Adverse events related to extraoperative invasive EEG monitoring with subdural grid electrodes: A systematic review and meta-analysis. *Epilepsia* **54**, 828–839 (2013).
6. M. Zijlmans, W. Zweiphenning, N. van Klink, Changing concepts in presurgical assessment for epilepsy surgery. *Nat. Rev. Neurol.* **15**, 594–606 (2019).
7. B. Frauscher *et al*., High-frequency oscillations: The state of clinical research. *Epilepsia* **58**, 1316–1329 (2017).
8. G. A. Worrell *et al*., High-frequency oscillations and seizure generation in neocortical epilepsy. *Brain* **127**, 1496–1506 (2004).
9. G. A. Worrell *et al*., High-frequency oscillations in human temporal lobe: Simultaneous microwire and clinical macroelectrode recordings. *Brain* **131**, 928–937 (2008).
10. A. Bragin, J. Engel Jr, C. L. Wilson, I. Fried, G. Buzsáki, High-frequency oscillations in human brain. *Hippocampus* **9**, 137–142 (1999).
11. K. Kobayashi *et al*., Scalp-recorded high-frequency oscillations in childhood sleep-induced electrical status epilepticus. *Epilepsia* **51**, 2190–2194 (2010).
12. L. P. Andrade-Valenca, F. Dubeau, F. Mari, R. Zelmann, J. Gotman, Interictal scalp fast oscillations as a marker of the seizure onset zone. *Neurology* **77**, 524–531 (2011).
13. M. Zijlmans *et al*., How to record high-frequency oscillations in epilepsy: A practical guideline. *Epilepsia* **58**, 1305–1315 (2017).
14. J. D. Jirsch *et al*., High-frequency oscillations during human focal seizures. *Brain* **129**, 1593–1608 (2006).
15. J. Jacobs *et al*., High-frequency electroencephalographic oscillations correlate with outcome of epilepsy surgery. *Ann. Neurol.* **67**, 209–220 (2010).
16. J. Y. Wu *et al*., Removing interictal fast ripples on electrocorticography linked with seizure freedom in children. *Neurology* **75**, 1686–1694 (2010).
17. M. A. van 't Klooster *et al*., Tailoring epilepsy surgery with fast ripples in the intraoperative electrocorticogram. *Ann. Neurol.* **81**, 664–676 (2017).
18. J. Jacobs *et al*., Interictal high-frequency oscillations (80-500 Hz) are an indicator of seizure onset areas independent of spikes in the human epileptic brain. *Epilepsia* **49**, 1893–1907 (2008).
19. T. Akiyama *et al*., Focal resection of fast ripples on extraoperative intracranial EEG improves seizure outcome in pediatric epilepsy. *Epilepsia* **52**, 1802–1811 (2011).
20. A. Thomschewski, A. S. Hincapié, B. Frauscher, Localization of the epileptogenic zone using high frequency oscillations. *Front. Neurol.* **10**, 94 (2019).

NEUROSCIENCE

21. A. H. Mooij, R. C. M. A. Raijmann, F. E. Jansen, K. P. J. Braun, M. Zijlmans, Physiological ripples (± 100 Hz) in spike-free scalp EEGs of children with and without epilepsy. *Brain Topogr.* **30**, 739–746 (2017).
22. C. G. Bénar, L. Chauvière, F. Bartolomei, F. Wendling, Pitfalls of high-pass filtering for detecting epileptic oscillations: A technical note on "false" ripples. *Clin. Neurophysiol.* **121**, 301–310 (2010).
23. P. Jiruska *et al*., Update on the mechanisms and roles of high-frequency oscillations in seizures and epileptic disorders. *Epilepsia* **58**, 1330–1339 (2017).
24. J. Engel Jr, A. Bragin, R. Staba, I. Mody, High-frequency oscillations: What is normal and what is not? *Epilepsia* **50**, 598–604 (2009).
25. J. Engel Jr, F. L. da Silva, High-frequency oscillations–Where we are and where we need to go. *Prog. Neurobiol.* **98**, 316–318 (2012).
26. J. Jacobs *et al*., Removing high-frequency oscillations: A prospective multicenter study on seizure outcome. *Neurology* **91**, e1040–e1052 (2018).
27. N. Gerner, A. Thomschewski, A. Marcu, E. Trinka, Y. Höller, Pitfalls in scalp high-frequency oscillation detection from long-term EEG monitoring. *Front. Neurol.* **11**, 432 (2020).
28. N. Roehri *et al*., High-frequency oscillations are not better biomarkers of epileptogenic tissues than spikes. *Ann. Neurol.* **83**, 84–97 (2018).
29. S. V. Gliske *et al*., Variability in the location of high frequency oscillations during prolonged intracranial EEG recordings. *Nat. Commun.* **9**, 2155 (2018).
30. S. Wang *et al*., Ripple classification helps to localize the seizure-onset zone in neocortical epilepsy. *Epilepsia* **54**, 370–376 (2013).
31. S. Wang *et al*., Interictal ripples nested in epileptiform discharge help to identify the epileptogenic zone in neocortical epilepsy. *Clin. Neurophysiol.* **128**, 945–951 (2017).
32. M. A. Kramer *et al*., Scalp recorded spike ripples predict seizure risk in childhood epilepsy better than spikes. *Brain* **142**, 1296–1309 (2019).
33. E. Boran, J. Sarnthein, N. Krayenbühl, G. Ramantani, T. Fedele, High-frequency oscillations in scalp EEG mirror seizure frequency in pediatric focal epilepsy. *Sci. Rep.* **9**, 16560 (2019).
34. N. E. van Klink *et al*., Ripples on rolandic spikes: A marker of epilepsy severity. *Epilepsia* **57**, 1179–1189 (2016).
35. D. Sun *et al*., High frequency oscillations relate to cognitive improvement after epilepsy surgery in children. *Clin. Neurophysiol.* **131**, 1134–1141 (2020).
36. A. B. Gardner, G. A. Worrell, E. Marsh, D. Dlugos, B. Litt, Human and automated detection of high-frequency oscillations in clinical intracranial EEG recordings. *Clin. Neurophysiol.* **118**, 1134–1143 (2007).
37. A. M. Spring *et al*., Interrater reliability of visually evaluated high frequency oscillations. *Clin. Neurophysiol.* **128**, 433–441 (2017).
38. N. von Ellenrieder, L. P. Andrade-Valença, F. Dubeau, J. Gotman, Automatic detection of fast oscillations (40-200 Hz) in scalp EEG recordings. *Clin. Neurophysiol.* **123**, 670–680 (2012).
39. C. J. Chu *et al*., A semi-automated method for rapid detection of ripple events on interictal voltage discharges in the scalp electroencephalogram. *J. Neurosci. Methods* **277**, 46–55 (2017).
40. D. Bernardo *et al*.; UCLA Pediatric Epilepsy Group; TACERN Study Group, Visual and semi-automatic non-invasive detection of interictal fast ripples: A potential biomarker of epilepsy in children with tuberous sclerosis complex. *Clin. Neurophysiol.* **129**, 1458–1466 (2018).
41. C. M. Michel, B. He, "EEG mapping and source imaging" in *Niedermeyer's Electroencephalography: Basic Principles, Clinical Applications, and Related Fields’*, D. L. Schomer, F. L. Da Silva, Eds. (Wolters Kluwer & Lippincott Williams & Wilkins, Philadelphia, ed. 7, 2017), pp. 1135–1156.
42. F. Pizzo *et al*., Deep brain activities can be detected with magnetoencephalography. *Nat. Commun.* **10**, 971 (2019).
43. S. Liu *et al*., Stereotyped high-frequency oscillations discriminate seizure onset zones and critical functional cortex in focal epilepsy. *Brain* **141**, 713–730 (2018).
44. S. Liu, J. Parvizi, Cognitive refractory state caused by spontaneous epileptic high-frequency oscillations in the human brain. *Sci. Transl. Med.* **11**, eaax7830 (2019).
45. T. Rasmussen, Characteristics of a pure culture of frontal lobe epilepsy. *Epilepsia* **24**, 482–493 (1983).
46. S. D. Lhatoo, P. Kahane, H. O. Lüders, *Invasive Studies of the Human Epileptic Brain: Principles and Practice* (Oxford University Press, 2018).
47. M. L. Scheuer, A. Bagic, S. B. Wilson, Spike detection: Inter-reader agreement and a statistical Turing test on a large data set. *Clin. Neurophysiol.* **128**, 243–250 (2017).
48. W. T. Blume, Clinical and electroencephalographic correlates of the multiple independent spike foci pattern in children. *Ann. Neurol.* **4**, 541–547 (1978).
49. N. Roehri, F. Pizzo, F. Bartolomei, F. Wendling, C. G. Bénar, What are the assets and weaknesses of HFO detectors? A benchmark framework based on realistic simulations. *PLoS One* **12**, e0174702 (2017).
50. F. Pizzo *et al*., Detectability of fast ripples (>250 Hz) on the scalp EEG: A proof-of-principle study with subdermal electrodes. *Brain Topogr.* **29**, 358–367 (2016).
51. N. van Klink, B. Frauscher, M. Zijlmans, J. Gotman, Relationships between interictal epileptic spikes and ripples in surface EEG. *Clin. Neurophysiol.* **127**, 143–149 (2016).
52. K. Kerber *et al*., Differentiation of specific ripple patterns helps to identify epileptogenic areas for surgical procedures. *Clin. Neurophysiol.* **125**, 1339–1345 (2014).
53. A. Matsumoto *et al*., Pathological and physiological high-frequency oscillations in focal human epilepsy. *J. Neurophysiol.* **110**, 1958–1964 (2013).
54. P. Modur, S. Miocinovic, Interictal high-frequency oscillations (HFOs) as predictors of high frequency and conventional seizure onset zones. *Epileptic Disord.* **17**, 413–424 (2015).
55. S. A. Weiss *et al*., Ripples on spikes show increased phase-amplitude coupling in mesial temporal lobe epilepsy seizure-onset zones. *Epilepsia* **57**, 1916–1930 (2016).
56. R. F. Helfrich, B. A. Mander, W. J. Jagust, R. T. Knight, M. P. Walker, Old brains come uncoupled in sleep: Slow wave-spindle synchrony, brain atrophy, and forgetting. *Neuron* **97**, 221–230.e4 (2018).
57. F. Melani, R. Zelmann, F. Dubeau, J. Gotman, Occurrence of scalp-fast oscillations among patients with different spiking rate and their role as epileptogenicity marker. *Epilepsy Res.* **106**, 345–356 (2013).
58. S. Kullback, R. A. Leibler, On information and sufficiency. *Ann. Math. Stat.* **22**, 142–143 (1951).
59. D. Dvorak, A. A. Fenton, Toward a proper estimation of phase-amplitude coupling in neural oscillations. *J. Neurosci. Methods* **225**, 42–56 (2014).
60. V. Brodbeck *et al*., Electroencephalographic source imaging: A prospective study of 152 operated epileptic patients. *Brain* **134**, 2887–2897 (2011).
61. V. V. Nikulin, G. Nolte, G. Curio, A novel method for reliable and fast extraction of neuronal EEG/MEG oscillations on the basis of spatio-spectral decomposition. *Neuroimage* **55**, 1528–1535 (2011).
62. S. Haufe, S. Dähne, V. V. Nikulin, Dimensionality reduction for the analysis of brain oscillations. *Neuroimage* **101**, 583–597 (2014).
63. R. D. Pascual-Marqui, Standardized low-resolution brain electromagnetic tomography (sLORETA): technical details. *Methods Find Exp. Clin. Pharmacol.* **24**, 5–12 (2002).
64. M. Seeber *et al*., Subcortical electrophysiological activity is detectable with high-density EEG source imaging. *Nat. Commun.* **10**, 753 (2019).
65. A. Sohrabpour, Y. Lu, G. Worrell, B. He, Imaging brain source extent from EEG/MEG by means of an iteratively reweighted edge sparsity minimization (IRES) strategy. *Neuroimage* **142**, 27–42 (2016).
66. C. Grova *et al*., Intracranial EEG potentials estimated from MEG sources: A new approach to correlate MEG and iEEG data in epilepsy. *Hum. Brain Mapp.* **37**, 1661–1683 (2016).
67. P. Krishnaswamy *et al*., Sparsity enables estimation of both subcortical and cortical activity from MEG and EEG. *Proc. Natl. Acad. Sci. U.S.A.* **114**, E10465–E10474 (2017).
68. A. J. Dobson, A. G. Barnett, *An Introduction to Generalized Linear Models* (Chapman and Hall/CRC, 2008).
69. A. Palmini *et al*., Intrinsic epileptogenicity of human dysplastic cortex as suggested by corticography and surgical results. *Ann. Neurol.* **37**, 476–487 (1995).
70. S. Liu *et al*., Exploring the time-frequency content of high frequency oscillations for automated identification of seizure onset zone in epilepsy. *J. Neural Eng.* **13**, 026026 (2016).
71. J. A. Blanco *et al*., Unsupervised classification of high-frequency oscillations in human neocortical epilepsy and control patients. *J. Neurophysiol.* **104**, 2900–2912 (2010).
72. M. Lévesque, A. Bortel, J. Gotman, M. Avoli, High-frequency (80-500 Hz) oscillations and epileptogenesis in temporal lobe epilepsy. *Neurobiol. Dis.* **42**, 231–241 (2011).
73. R. Zelmann, J. M. Lina, A. Schulze-Bonhage, J. Gotman, J. Jacobs, Scalp EEG is not a blur: It can see high frequency oscillations although their generators are small. *Brain Topogr.* **27**, 683–704 (2014).
74. N. Kuhnke *et al*., High frequency oscillations in the ripple band (80-250 Hz) in scalp EEG: Higher density of electrodes allows for better localization of the seizure onset zone. *Brain Topogr.* **31**, 1059–1072 (2018).
75. Y. Lu *et al*., Noninvasive imaging of the high frequency brain activity in focal epilepsy patients. *IEEE Trans. Biomed. Eng.* **61**, 1660–1667 (2014).
76. N. von Ellenrieder *et al*., Detection and magnetic source imaging of fast oscillations (40-160 Hz) recorded with magnetoencephalography in focal epilepsy patients. *Brain Topogr.* **29**, 218–231 (2016).
77. J. Velmurugan *et al*., Magnetoencephalography imaging of high frequency oscillations strengthens presurgical localization and outcome prediction. *Brain* **142**, 3514–3529 (2019).
78. S. Yuval-Greenberg, O. Tomer, A. S. Keren, I. Nelken, L. Y. Deouell, Transient induced gamma-band response in EEG as a manifestation of miniature saccades. *Neuron* **58**, 429–441 (2008).
79. C. Alvarado-Rojas *et al*., Different mechanisms of ripple-like oscillations in the human epileptic subiculum. *Ann. Neurol.* **77**, 281–290 (2015).
80. M. Valero *et al*., Determinants of different deep and superficial CA1 pyramidal cell dynamics during sharp-wave ripples. *Nat. Neurosci.* **18**, 1281–1290 (2015).
81. R. J. Staba *et al*., Increased fast ripple to ripple ratios correlate with reduced hippocampal volumes and neuron loss in temporal lobe epilepsy patients. *Epilepsia* **48**, 2130–2138 (2007).
82. A. Bragin *et al*., Interictal high-frequency oscillations (80-500 Hz) in the human epileptic brain: Entorhinal cortex. *Ann. Neurol.* **52**, 407–415 (2002).
83. G. Buzsáki, Z. Horváth, R. Urioste, J. Hetke, K. Wise, High-frequency network oscillation in the hippocampus. *Science* **256**, 1025–1027 (1992).
84. M. Zijlmans, J. Jacobs, R. Zelmann, F. Dubeau, J. Gotman, High-frequency oscillations mirror disease activity in patients with epilepsy. *Neurology* **72**, 979–986 (2009).
85. Y. Sato *et al*., Preictal surrender of post-spike slow waves to spike-related high-frequency oscillations (80-200 Hz) is associated with seizure initiation. *Epilepsia* **55**, 1399–1405 (2014).
86. H. Blumenfeld, Cellular and network mechanisms of spike-wave seizures. *Epilepsia* **46**, 21–33 (2005).
87. J. Pallud *et al*., Cortical GABAergic excitation contributes to epileptic activities around human glioma. *Sci. Transl. Med.* **6**, 244ra89 (2014).
88. H. Jiang, Z. Cai, G. A. Worrell, B. He, Multiple oscillatory push-pull antagonisms constrain seizure propagation. *Ann. Neurol.* **86**, 683–694 (2019).
89. A. Sohrabpour *et al*., Noninvasive electromagnetic source imaging of spatiotemporally distributed epileptogenic brain sources. *Nat. Commun.* **11**, 1946 (2020).
90. H. Miyamoto *et al*., Impaired cortico-striatal excitatory transmission triggers epilepsy. *Nat. Commun.* **10**, 1917 (2019).
91. H. G. Wieser *et al*.; Commission on Neurosurgery of the International League Against Epilepsy (ILAE), ILAE Commission Report. Proposal for a new classification of outcome with respect to epileptic seizures following epilepsy surgery. *Epilepsia* **42**, 282–286 (2001).
92. R. L. Thorndike, Who belongs in the family? *Psychometrika* **18**, 267–276 (1953).
93. M. X. Cohen, Comparison of linear spatial filters for identifying oscillatory activity in multichannel data. *J. Neurosci. Methods* **278**, 1–12 (2017).
94. C. Grova *et al*., Evaluation of EEG localization methods using realistic simulations of interictal spikes. *Neuroimage* **29**, 734–753 (2006).
95. N. Otsu, A threshold selection method from gray-level histograms. *IEEE Trans. Syst. Man Cybern.* **9**, 62–66 (1979).
96. H. Hentschke, M. C. Stüttgen, Computation of measures of effect size for neuroscience data sets. *Eur. J. Neurosci.* **34**, 1887–1894 (2011).
97. P. Berens, CircStat: A MATLAB toolbox for circular statistics. *J. Stat. Softw.* **31**, 1–21 (2009).